THE JOURNAL OF PHYSICAL CHEMISTRY C

Article

pubs.acs.org/JPCC

Elastic and Vibrational Properties of α- and β-PbO.

P. Canepa,*[,†,‡] P. Ugliengo,[§] and M. Alfredsson[†]

[†]School of Physical Sciences, Ingram building, University of Kent, Canterbury CT2 7NH, United Kingdom

[‡]Department of Physics, Wake Forest University, 1834 Wake Forest Road, Winston-Salem, North Carolina 27109, United States

[§]Dipartimento di Chimica, University of Torino, Via Pietro Giuria 7, Turin, 10125, Italy

Supporting Information

ABSTRACT: The structure, electronic, and dynamic properties of the two-layered α (litharge) and β (massicot) phases of PbO have been studied by density functional methods. The role of London dispersion interactions as leading component of the total interaction energy between layers has been addressed by using the Grimme's approach in which new parameters for Pb and O atoms have been developed. Both gradient-corrected and hybrid functionals have been adopted using Gaussian-type basis sets of polarized triple-ζ quality for O atoms and small-core pseudopotential for the Pb atoms. Basis set superposition error (BSSE) has been accounted for by the Boys–Bernardi correction to compute the interlayer separation. Cross-checks with calculations adopting plane waves that are BSSE free have also been performed for both structures and vibrational frequencies. With the new set of proposed Grimme's type parameters, structures and dynamical parameters for both PbO phases are in good agreement with experimental data.

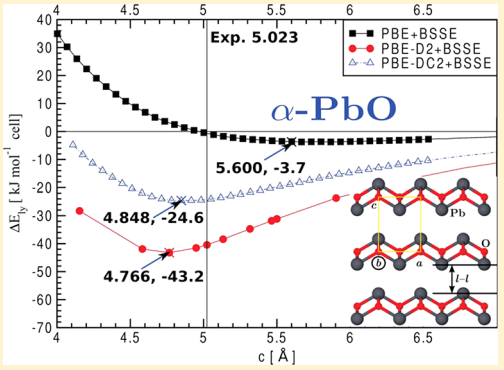

1. INTRODUCTION

Lead monoxide (PbO) is largely employed for several industrial and techological applications such as electronic devices,[1−3] in special ceramic glasses,[4,5] for X-ray cathodes, for pigments,[6,7] in rubber vulcanization,[8,9] and in the automotive sector as an essential component for batteries.[10,11] PbO is largely found in two polymorphs: a tetragonal $P4/nmm$ phase (α-PbO or litharge) and an orthorhombic phase $Pbcm$ (β-PbO or massicot).

In α-PbO, the Pb^{2+} ions are pyramidally coordinated by oxygen atoms (see Figure 1a) packed in a special layered arrangement that resembles a distorted CsCl structure. This distortion is principally caused by free lone pairs on the Pb^{2+} ions. The key element in the lone pair localizations is the hybridization of the Pb(6s) and Pb(6p) orbitals with O(2p) states as demonstrated by Watson and co-workers.[12,13] Below 200 K, the tetragonal α-PbO undergoes a phase transition to orthorhombic $Cmma$ as observed by Boher et al.,[14] where the new a' and b' lattice parameters are redefined as $a' \approx a + b$, $b' \approx b - a$, where a and b are α-PbO lattice constants. The distorted α-phase can be regarded as intermediate PbO phase between α- and β-polymorphs. Very few studies are available on β-PbO. This lead oxide polymorph is characterized by zigzag chains of PbO units repeated along the b axis of the cell (see Figure 1b). As for litharge, Pb^{2+} ions are found pyramidally coordinated by oxygen atoms although forming squares parallel to the bc plane. The zigzag chains are then stacked along the a axis forming a layered structure almost unique in nature. While previous theoretical works established the structure of both PbO polymorphs[15−17] and the nature of the Pb lone pairs,[18] in this study, we also address the role of dispersion interactions on the energetic, structure, and dynamic properties of both phases.

As depicted in Figure 1 in both lead oxide polymorphs, rippled two-dimensional planes are stacked in a peculiar layered arrangement. The layered nature of α- and β-PbO suggests that dispersive interactions may play a key role in stabilizing these structures.

Differently from classic post-Hartree–Fock methods such as MP2 and CCSD(T), most common density functional theory (DFT)-GGA and hybrid functionals are unable to deal with purely dispersive London forces originating from fluctuating dipole–dipole interactions. Currently, there are three main approaches to include dispersive forces in DFT:[19] (1) the design of new functionals derived in a fully ab initio fashion as suggested by Dion et al.;[20−23] (2) highly parametrized functionals of the M0X family as propsed by Zhao and co-workers;[24,25] and (3) an empirical correction to the standard DFT energy and gradient on the basis of the empirical London formula as reproposed by Grimme[26,27] and later improved by Tkatchenko and co-workers.[26−30] In this latter scheme, hereafter termed DFT-D2 (Grimme's correction),[26,27] an atom–atom empirical potential (of the form $f(R)C_6/R^6$) accounts for the dispersion on the DFT energy as follows:

$$E_{DFT-D2} = E_{DFT} + E_D \quad (1)$$

where E_D is the additive dispersion term.

Received: April 17, 2012
Revised: September 10, 2012
Published: September 12, 2012

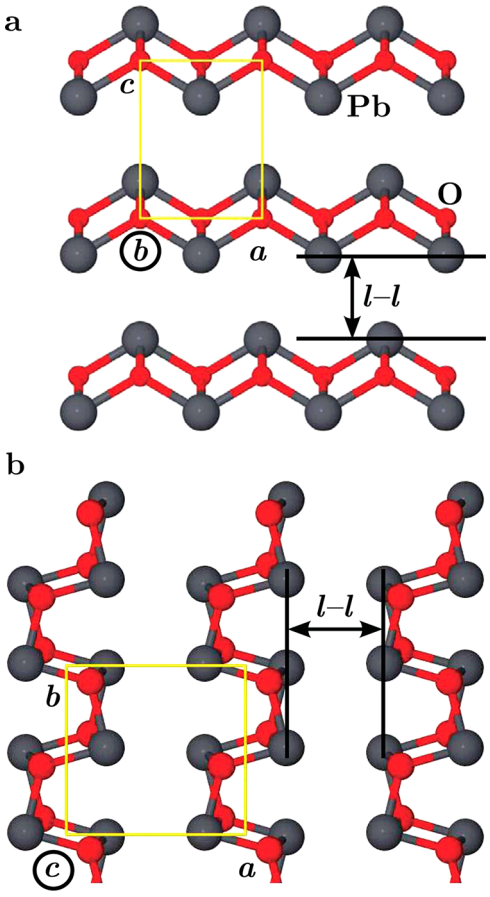

Figure 1. (a) View along the [010] direction of α-PbO ($P4/nmm$) and (b) along the [001] direction β-PbO ($Pbcm$). The interlayer distance is highlighted as l–l.

2. COMPUTATIONAL DETAILS

Simulations presented here were performed with CRYSTAL09[31,32] using hybrid and plain functionals. We used three GGA functionals: PBE,[33] PBEsol,[34] and BLYP[35,36] and two hybrid-GGA functionals: B3LYP[35−37] (20% HF exchange) and PBE0[38] (25% HF). Oxygen atoms were described with an all-electron basis set TPZ by Schafer et al. (see ref 39). Pb core−electrons were described by an effective small core potential[40] along with a VDZ basis set for the valence shells.[41] We used a Monkhorst-Pack[42] grid of 8 × 8 × 8 k-points ensuring that the total energy was well converged. The self-consistent-field (SCF) procedure was converged within 10^{-8} Hartree. The Coulomb and the exchange series were truncated using stringent overlap criteria, that is, 10^{-9}, 10^{-9}, 10^{-9}, 10^{-9}, and 10^{-12}.

Second-order elastic constants, $C_{i,j}$, were evaluated using the analytic total energy gradient and numerical second derivative with respect to the applied strain around the optimized equilibrium structure.[43] According to the symmetry of the second-order elastic strain tensor, the appropriate number of strains were applied; hence, the internal coordinates were relaxed for each strain displacement. Bulk moduli were determined via the elastic constants (for tetragonal Voight averages: $^1/_9(2C_{11} + 2C_{12} + 4C_{13} + C_{33})$ and for orthorhombic: $^1/_9((C_{11} + C_{22} + C_{33}) + 2(C_{12} + C_{13} + C_{23}))$). For these calculations, we reduced the SCF tolerance to 10^{-9} Hartree, whereas those on the gradient and the root mean square (rms) displacement were 6 × 10^{-5} and 1.2 × 10^{-4} Hartree bohr^{-1}, respectively.[43] For phonon calculation the dynamical matrix, at the Γ point, was computed by finite differences: the atomic displacement was set to 3 × 10^{-3} Å reducing the SCF tolerance to 10^{-11} Hartree.[44]

Aware of the spurious basis set superposition error (BSSE) introduced by the linear combination of atomic orbitals (LCAO) treatment employed by CRYSTAL09, we performed some PBE-D2 and -DC2 (see section 3) calculations with a pseudopotential plane-wave (PP-PW) code *PWscf* (a Quantum ESPRESSO package),[45] which is BSSE free. We used ultrasoft pseudopotentials for Pb (fully relativistic and with spin−orbit coupling correction) and O, whereas the remaining valence electrons were described with a plane-wave basis set with a cutoff of 950 eV, while the total energy was sampled over a 8 × 8 × 8 k-point grid. Where not explicitly stated, results were produced using CRYSTAL09.

Structure manipulation and representation were carried out with J-ICE.[46]

3. DISPERSIVE FORCES

The empirical dispersion contribution E_D of eq 1 is defined as

$$E_D = -s_6 \sum_g \sum_{ij} \frac{C_6^{ij}}{R_{ij,g}^6} f_{dmp}(R_{ij,g}) \tag{2}$$

where the summations extend over all atomic pairs i,j and g lattice vectors. C_6^{ij} is the dispersion coefficient, and $s_6 = 0.75$ is a functional dependent scaling factor (see ref 27). $R_{ij,g}$ is the interatomic distance between atoms i in the reference cell and j in the neighboring cells at distance $|g|$. All pairs farther than 25 Å are disregarded in the summations because of their negligible contribution. Double counting for small interatomic distances is avoided using the following damping function $f_{dmp}(R_{ij,g}) = 1/(1 + e^{-d(R_{ij,g}/R_{vdW}-1)})$ where R_{vdW} is the atomic van der Walls' radii and d is the damping function steepness ($d = 20$).[26] In Grimme's work, R_{vdW} is set as the atomic van der Waals radii, which are 1.767 and 1.342 Å for Pb and O, respectively. The definition of the C_6^{ij} coefficients of eq 3a[27] follows the well-known geometrical mean

$$C_6^{ij} = \sqrt{C_6^i C_6^j} \tag{3a}$$

$$C_6^i = 0.05 N I_p^i \alpha^i \tag{3b}$$

In eq 3b, N is the number of the shell electrons and has values of 2, 10, 18, 36, 54, and 72 for atoms from rows 1−6 of the periodic table. The original Grimme's[27] C_6^i parameters were derived from the atomic polarizabilites, α^i, and ionization energies, I_p^i,[26,27] leading to 63.16 for Pb and 0.7 Jnm^6 mol^{-1} for O, respectively. The C_6^i parameters for heavy elements (e.g., Sn, Pb) were simply extrapolated from those of lighter elements of the same group[26,27] resulting in rather approximated values. Furthermore, the electronic nature (covalence or ionicity) of atomic species varies depending on the local chemical environment imposing some limitations in the use of the atomic-like parameters. To give a better estimation of the C_6^i values, one should find a way to account for the different chemical environments of a given atomic species. Different methods to reparametrize the C_6^i for ionic systems have been proposed,[47,48] but the C_6^i values were derived ad hoc for each system reducing their transferability. In this study, we derive the C_6^i parameters for each ionic species in an ab initio fashion following as close as possible the protocol suggested by

dx.doi.org/10.1021/jp3036988 | J. Phys. Chem. C 2012, 116, 21514−21522

Table 1. Lattice Parameters *a*, *b*, and *c* (in Å), *c*/*a* Ratio, Volume (in Å^3) and Interlayer *l*–*l* Distance (See Figure 1, in Å) of *α*-, *β*-PbO[a]

α-PbO *P4/nmm*	*a*	*c*	V	*c*/*a*	*l*–*l*
exp[b]	3.975	5.023	39.7	1.263	2.6
PBE[c]	4.097	5.096 (5.600)	41.9	1.221 (1.367)	3.0
PBE-PW[d]	3.985	5.579	45.8	1.400	3.2
PBE-D2[c]	4.049	4.584 (4.766)	37.6	1.132 (1.180)	2.4
PBE-D2-PW[d]	3.985	4.762	37.8	1.195	2.4
PBE-DC2[c]	4.066	4.648 (4.848)	38.4	1.143 (1.192)	2.5
PBE-DC2-PW[d]	3.980	4.835	38.9	1.215	2.5
PBEsol[c]	4.035	4.690	38.2	1.162	2.3
PBE0[c]	4.021	4.996	40.4	1.242	2.6
BLYP[c]	4.144	5.746	49.3	1.386	3.3
B3LYP[c]	4.073	5.691	47.2	1.397	3.3
LDA-PZ[e]	3.956	4.874	38.1	1.232	-
LDA-PZ[f]	3.953	4.988	-	-	-
LDA-PZ[g]	3.910	4.930	-	-	-
β-PbO *Pbcm*	*a*	*b*	*c*	V	*l*–*l*
exp[h]	5.893	5.490	4.753	153.8	3.2
PBE[c]	6.213	5.587	4.823	167.4	3.5
PBE-PW[d]	6.293	5.805	4.800	147.9	3.6
PBE-D2[c]	5.499	5.324	4.732	145.3	2.8
PBE-D2-PW[d]	5.541	5.388	4.846	144.7	2.8
PBE-DC2[c]	5.688	5.413	4.836	148.9	2.9
PBE-DC2-PW[d]	5.636	5.445	4.836	148.4	2.9
PBEsol[c]	5.962	5.302	4.762	150.5	3.2
PBE0[c]	6.174	5.586	4.704	162.2	3.4
BLYP[c]	6.554	5.868	4.879	187.7	3.8
B3LYP[c]	6.471	5.798	4.791	179.8	3.7
LDA-PZ[g]	5.770	5.380	4.680	-	-

[a]Data in brackets are BSSE corrected. [b]Reference 51, X-ray. [c]This work, LCAO. [d]This work, PP-PW. [e]References 12 and 13, PP-PW. [f]Reference 18, PP-PW. [g]Reference 16, augmented spherical waves. [h]Reference 52, X-ray.

Grimme by enforcing the role of the specific environment for each atomic species (details in the Supporting Information). On elementary considerations, the net charges of the Pb and O ions should be +2 and −2, respectively. Mulliken analysis, albeit quite dependent on the adopted basis set, gives much reduced values of +1 and −1, respectively. Nevertheless, Löwdin charges calculated using a PP-PW approach agree with the Mulliken's picture. Using a pragmatic approach, we compute the ionization potential and the polarizability for the bare Pb^+ and Pb^{2+} ions using a Stuttgart ECP with a QVZ basis set. The same methodology cannot be adopted for computing these quantities for O^- and O^{2-} because both species are unstable with respect to the free atom. In the latter case, we have adopted a method proposed for MgO by Tosoni and Sauer[49] to set up a proper environment for oxygen in order to get both O^- and O^{2-} as stable species. As described in the Supporting Information, we average the values of the polarizabilities over the two Pb^+/Pb^{2+} and O^-/O^{2-} states to account for the semi-ionic nature of the PbO oxides. Because the ionization potentials are intrinsically discontinuous variables, we choose to adopt the values for the Pb^{2+} and O^{2-} to be used in the definition of the dispersion coefficient C_6^i. Within this assumption, the final C_6^i values with eq 3b for Pb and O become 36.93 and 0.54 Jnm mol^{-1}, respectively (see Supporting Information). The new C_6^i values are smaller than the atomic-like ones reported by Grimme.[27] The geometrical mean of the single C_6^i parameters (see eq 3a) results in a mean C_6 (PbO) equal to 4.48 Jnm mol^{-1}, which is found smaller than that proposed by Grimme,[27] that is, 6.64 Jnm mol^{-1}, avoiding the occurrence of spurious overbinding effects. In summary, two kinds of DFT-D2 were employed: (1) using the Grimme's[27] parameters (PBE-D2) and (2) using the recalculated C_6^i (PBE-DC2) according to the scheme presented here. Results are shown in Table 1.

4. RESULTS AND DISCUSSION

Results are outlined through three thematic sections: in section 4.1, we address the description of the geometrical properties of the PbO phases while discussing the effect of dispersion on these materials. This section terminates with an insightful investigation of the lone-pair nature using the electric field gradient. Section 4.2 discusses the elastic properties, while section 4.3 discusses vibrational frequencies.

4.1. Geometry. Both *α*- and *β*-PbO polymorphs crystallize in a layered arrangement.[12,13,16−18,50] The PbO layered stacking and the interlayer distances (*l*–*l*, see Figure 1) are controlled by lone pairs on the Pb sites. The resulting deformed electron cloud (of Pb^{2+}) produces an electric dipole that along with dispersion forces collectively drives the layers to stack. The structures of Table 1 were obtained after full structural relaxation (at 0 K) from experimental X-ray data of the PbO phases.[51,52]

Table 1 shows how the LCAO method reproduces with good accuracy both the experimental[51,52] and the previous local density approximation DFT (LDA-DFT) data.[12,13,16−18,50] With PBE, we found the *α* phase more stable than the *β* one consistently with experimental evidence (ΔE = 3.22 kJ mol^{-1} per formula unit). On the other hand, the distorted *α* phase, observed at low temperature, is negligibly more stable (at the

dx.doi.org/10.1021/jp3036988 | J. Phys. Chem. C 2012, 116, 21514−21522

PBE level) than the α one for about 0.040 kJ mol^{-1} per formula unit.

Among the GGA functionals, PBE is by far more accurate than BLYP; the latter largely overestimates the l–l distance together with the lattice parameters a and c. Eventually, B3LYP and PBE0 further increase the magnitude of the lattice parameters (see Table 1). α-PbO turns into β-PbO at 4.15 GPa with PBE (2.80 GPa with LDA), while experimental data ranges from 3.0 up to 3.6 GPa.[53] From this preliminary evaluation, PBE appears to be the best choice, and therefore, it will be used to discuss the dispersion effects throughout the paper. Unsurprisingly, functionals based on the Becke exchange (BLYP and B3LYP) show an overrepulsive behavior compared to Perdew's functionals (PBE, PBE0) in agreement with ref 54.

4.1.1. The Effect of the Dispersion. While dispersion is accounted for in both phases, the detailed discussion only concerns α-PbO. Insights on the layered structure of PbO is given by ΔE_{ly}, which determines the extent of the interaction between two PbO sublayers

$$\Delta E_{ly} = E_c - E_\infty \tag{4}$$

where E_c is the energy of two PbO layers, with atoms in the same geometrical relationships as in the bulk structure, at a given interlayer distance (see l–l in Figure 1), and E_∞ is the energy of two PbO layers well separated and noninteracting. ΔE_{ly} is the energy cost of extracting a PbO sheet from the bulk (see Figure 1). Practically, this is done by running several SCF points at increasing lattice parameters (i.e., c for α-PbO) eventually affecting the l–l distance between two PbO layers. The real effect of the dispersion contribution, introduced by DFT-D2 or DFT-DC2, should only affect the ΔE_{ly} magnitude. Figure 2 shows the behavior of ΔE_{ly} at increasing lattice parameters c in α-PbO.

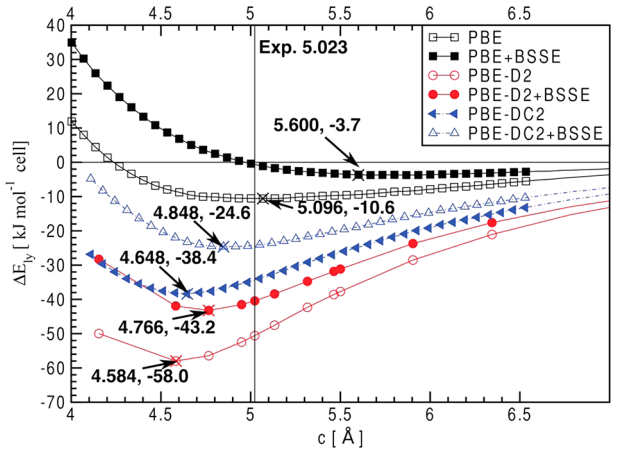

Figure 2. ΔE_{ly} versus c for α-PbO using PBE, PBE-D2, and PBE-DC2. ΔE_{ly} is in kJ mol^{-1} and c is in Å. The current graph is shortened at 7 Å, but SCF calculations were run up to 40 Å (c) where ΔE_{ly} is null.

In Figure 2, ΔE_{ly} changes dramatically when the D correction is introduced (see both PBE-D2 and PBE-DC2 cases). The PBE curve presents a very shallow minimum of −10.6 kJ mol^{-1}. The correction introduced on E_{ly} by PBE-D2, −58.0 kJ mol^{-1}, is 47.4 kJ mol^{-1} with respect to plain PBE. The PBE-DC2 data lies between the PBE and the PBE-D2 curves (−38.4 kJ mol^{-1}, see Figure 2). The empirical dispersion term, E_D of eq 1 and eq 2, of the total energy promotes the interlayer interaction forcing a decrease in the interlayer spacing. In α-PbO, the reduction of the c lattice constant is clear evidence of an increase in the layer–layer interaction. The final magnitude relies totally on the size of the C_6^i parameters that enter eq 2.

The large binding contribution of PBE-D2 and PBE-DC2 is affected by the BSSE. The BSSE has a twofold effect: (1) it reduces the relative ΔE_{ly} (i.e., shifting the binding curve to more negative ΔE_{ly} values overbinding the PbO layers) and (2) it artificially reduces the magnitude of c. The BSSE was calculated using the counterpoise correction and was practically done by introducing ghost functions on the two PbO layers while they were progressively separated. Knowing the magnitude of the BSSE, one can recalculate the corrected dispersion curve, whose minimum results shifted from the noncorrected one. The PBE BSSE corrected c value is 5.600 Å, which is largely overestimated with respect to the experimental value (see Table 1, data in parentheses). Calculations with the PBE functional using *PWscf* (BSSE free) confirmed our findings with the LCAO method.

Summarizing, the PBE functional largely overestimates the lattice parameters involved in the stacking process. All LCAO data of Table 1 when corrected for BSSE are shifted to larger values. PBE-D2 overbinds the α-PbO structure (c = 4.584 Å, see Table 1), whereas when corrected for the BSSE, the c value (4.766 Å) moves toward the experimental value (5.023 Å) but is still underestimated. This is confirmed by the PP-PW calculations. On the other hand, the reparametrization of Grimme's coefficients introduces a visible improvement in the geometry description of α-PbO. The c value (after correcting for the BSSE) is found in better agreement with the experimental value (4.848 Å). This also agrees with PP-PW calculations (c = 4.835 Å). With PBE-DC2, α-PbO is more stable than the β phase by 3.6 kJ mol^{-1} per formula unit and is also comparable with the PBE value 3.2 kJ mol^{-1} per formula unit. This shows that dispersion is very similar for the two PbO phases. Although we did not calculate the ΔE_{ly} for the β polymorph, a very similar behavior of Figure 2 is expected. In the next sections, only data obtained with PBE and PBE-DC2 will be considered disregarding the PBE-D2.

Although the reproduction of band gap is not appropriate with DFT, the introduction of the dispersion reduces the band gap simply through the decrease of the c parameter, which for α-PbO is 2.9 eV with PBE and is 2.8 eV with PBE-DC2 and is 2.2 eV with PBE-D2. As observed by Allen et al.,[48] the band gap decrease is concomitant with the reduction of the c parameter. This is the only effect noticeable by looking at the band structure and density of states plots (not reported here).

4.1.2. Electric Field Gradient and Quadrupole Coupling Constants. The electric field gradient tensor (EFG) is beneficial to understand how the PbO lone pairs arrange within the interlayer space (see distance l–l in Figure 1).[55] EFG components V_{11}, V_{22}, and V_{33} are ordered according to their magnitudes $V_{11} \leq V_{22} < V_{33}$. Relevant is the EFG asymmetry, η, calculated as $\eta = (|V_{22}| - |V_{11}|)/|V_{33}|$, whereas the quadrupole coupling constant (QCC) is computed from V_{33}:

$$\mathrm{QCC} = \frac{e^2 q_m Q}{h} = \frac{eQV_{33}}{h} \tag{5}$$

with e the electron charge and Q the atomic quadrupole moment.

EFG tensor components, η, and QCC values for ^{17}O and ^{204}Pb are shown in Table 2 and Figure 3.

dx.doi.org/10.1021/jp3036988 | J. Phys. Chem. C 2012, 116, 21514–21522

Table 2. PBE EFG Components, η, and QCC for the Following Nuclei: ^{17}O and ^{204}Pb of α- and β-PbO[a]

Z	V_{11}	V_{22}	V_{33}	QCC	η
			α-PbO *P4/nmm*		
Pb[b]	−5.00	−5.00	10.00	104.17	0.00
O[c]	−1.88	−1.88	3.76	1.13	0.00
			β-PbO *Pbcm*		
Pb[b]	−3.16	−9.32	12.50	130.21	0.16
O[c]	−0.49	1.14	2.14	0.64	0.06

[a]Z is for nucleus. V_{xx} is expressed in 10^{-1} e au^{-3} (1 e au^{-3} = 9.717 × 10^{21} Vm^{-2}); QCC is in MHz. [b]Reference 56, experimental $Q(^{204}Pb)$ = 4.42 × 10^{-29} m^2. [c]Reference 57, experimental $Q(^{17}O)$ = −2.56 × 10^{-30} m^2.

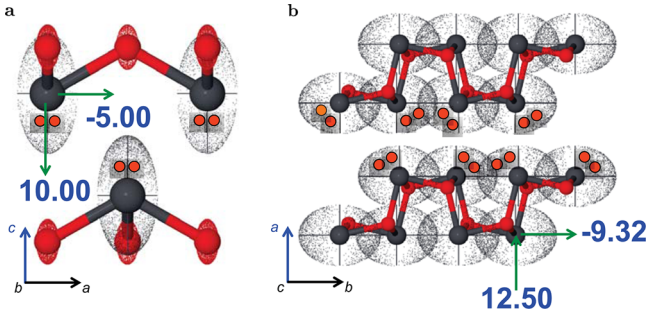

Figure 3. EFG principal components (arrows) superimposed on the two PbO structures (a) α and (b) β. V_{11}, V_{22}, and V_{33} refer to data in Table 2 and are in 10^{-1} e au^{-3}. Orange circles represent the lone pairs within the interlayer zone.

V_{33} in α-PbO confirms that the lone pair is oriented along the *c* axis as previously observed with electron localization functions (ELF) plots.[18] The lone pair of Pb atoms in the β-phase is found at an angle of 125.9, 38.2, and 101.5° with respect to lattice constants *a*, *b*, and *c*. Differently from the α-phase in β-PbO, the Pb lone pairs are not entirely oriented in one direction, and similar evidence was discussed by Rault et al.[18]

Friedemann et al.[56] affirmed that the QQC for the β-polymorph (158.96 MHz) is larger than the corresponding QCC (96.82 MHz) value in the α-phase, which agrees with our results. Our ab initio data is also confirmed by LAPW simulations (β-QQC, 151.55; α-QCC, 93.55 MHz).[56] Le Bellac et al.[58] also observed that the phase transition $\alpha \rightarrow \beta$ is accompanied by an evident change in orientation of the lone pair. PBE-DC2 EFG components are equal to those calculated with plain PBE showing that dispersion interactions are too weak to alter the component of the electron density at nuclei.

4.2. Elastic Properties. Table 3 shows the elastic constants and bulk moduli of α- and β-PbO calculated with the PBE and PBE-DC2 functionals.

Bulk moduli of Table 3 are very similar to previous LDA simulations and experimental value in the case of α-PbO[12,13,17,53] confirming the soft nature of these materials. Previous LDA simulations[12,13] behave significantly better than our PBE results. Bulk moduli for the β-phase are in closer agreement with the LDA data. Although the calculated elastic constants are consistent with the geometries of the PbO phases, the experimental values are currently not available. For α-PbO, C_{11} and C_{22} (64.7 GPa) are larger than C_{33} (16.3 GPa) suggesting that the distortion along the [001] direction is easier (see Table 3), which agrees with the layered structure. The inverse trend is obtained for α-PbO shear stresses. The effect exerted by the lone pair on β-PbO is smaller than in the α-phase; in fact, C_{11} (42.1 GPa) acting orthogonally to the [100] direction (i.e., the *a* direction) is similar to C_{22} (45.5 GPa), which acts along the zigzag chains. The strain along the C_{33} (96.6 GPa) remains the hardest one according to the structural arrangement. Mixed strains (C_{12}, C_{13}, and C_{23}) and pure shear stresses (C_{44}, C_{55}, and C_{66}) are consistent with the geometry definition of both lead oxide phases. We observed that PbO macroscopic densities increase when the α phase is irreversibly transformed into its β one. Bulk moduli and elastic constants calculated with PBE-DC2 are similar to PBE. PBE-DC2 improves the bulk modulus of α PbO toward the experimental value.

4.3. Phonon Frequencies at the Γ Point. Γ point phonon frequencies were computed by using PBE and PBE-DC2. The relevant infrared (IR), Raman frequency window for both monoxides is relatively narrow: 100−500 cm^{-1}.[59] This is likely to cause overlapping between near bands as confirmed by Adams and Stevens.[59] α-PbO with space group *P4/nmm* (D_{4h}^7) gives rise to nine vibrational modes (see eq 6a). The PbO-β phase *Pbcm* (D_{2h}^{11}) shows 21 vibrational modes (see eq 6b).

$$\Gamma^{\alpha} = A_{1g} + A_{2g} + B_{1g} + B_{2g} + 2E_g + A_{1u} + A_{2u} + B_{2u} + 2E_u \quad (6a)$$

$$\Gamma^{\beta} = 3B_{2u} + 4B_{1g} + 4A_g + 2B_{2g} + 3B_{3u} + 2A_u + B_{1u} + 2B_{3g} \quad (6b)$$

Vibrational frequencies calculated within the LCAO approximation are intrinsically affected by the BSSE error. To understand the magnitude of the BSSE on the final result, we have compared the IR/Raman frequencies computed with

Table 3. PBE, PBE-DC2 Elastic Constants C_{ij}, and Bulk Moduli B (Calculated via Elastic Constants) in GPa for α- and β-PbO

	C_{11}	C_{22}	C_{33}	C_{44}	C_{55}	C_{66}	C_{12}	C_{13}	C_{23}	B
					α-PbO *P4/nmm*					
PBE[a]	64.7	64.7	16.3	10.9	10.9	54.4	64.6	14.7	14.7	36.9
PBE-DC2[a]	53.2	53.2	30.2	18.7	18.7	44.2	51.3	20.0	20.0	35.5
LDA[b]										24.0
exp[c]										23.1
					β-PbO *Pbcm*					
PBE[a]	42.1	45.5	96.6	39.8	7.8	1.8	6.9	11.9	27.0	30.6
PBE-DC2[a]	48.4	47.3	102.2	30.6	22.5	2.9	7.2	12.8	25.4	32.1
LDA[d]										31.1

[a]This work, LCAO. [b]References 12 and 13, PP-PW. [c]Reference 53, exp. [d]Reference 17, PP-PW.

dx.doi.org/10.1021/jp3036988 | J. Phys. Chem. C 2012, 116, 21514−21522

Table 4. IR, Raman (R) Frequencies, in cm^{-1}, of α-PbO[a]

		ν					$\Delta\nu$		IR int.	
irep.	A	PBE	PBE-DC2	LDA[b]	E IR[c]	E R[c]	PBE	PBE-DC2	PBE	PBE-DC2
E_g	R	405	413			321	84	92		
A_{2u}	IR	387	366	399	470		−83	−104	655	810
B_{1g}	R	332	340			338	−6	2		
E_u	IR	230	264	275	243		−13	21	2269	2789
A_{1g}	R	149	154			146	3	8		
E_g	R	79	101			81	−2	22		

[a]Simulated intensities are only available for IR modes (in km mol^{-1}). Irep. is for irreducible representation, A is for activity, int. is for intensity, and E is for experimental. Experimental IR and Raman frequencies were measured by Adams and Stevens,[59] while theoretical data is only available for IR.[50] Whenever the experimental data is available, $\Delta\nu$ is calculated from this value. [b]Reference 50, PP-PW. [c]Reference 59, single crystal specimen at 295 K.

Gaussian basis set calculations with those obtained with a PP-PW approach (i.e., *PWscf*). Results reported in the Supporting Information show a good agreement between the two data sets implying that BSSE does not dramatically affect the vibrational frequencies.

4.3.1. α-PbO. Of the nine modes of α-PbO, two are IR active (A_{2u} and E_u); the Raman spectrum consists of four modes (A_{1g}, B_{1g}, and $2E_g$). E modes degenerate showing the same atomic displacements but are orthogonal to one another. Table 4 compares the calculated IR and Raman frequencies with the experimental data, and their graphical representation is shown in Figure 4.

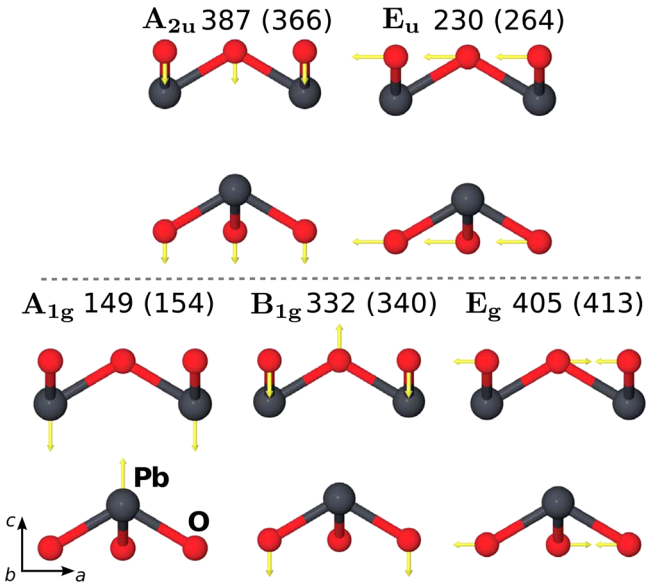

Figure 4. Active IR (on the top part) and Raman (on the bottom part) modes for α-PbO in cm^{-1}. Only one degeneracy is shown for vibrational modes classified as E. PBE-DC2 values are in brackets.

Raman modes A_{1g} and B_{1g} involve only the motion of lead and oxygen atoms parallel to the *c* axis, while the A_{2u} mode is an antiphase motion of Pb and O atoms. E_u and $2E_g$ show atomic displacements in the *ab* planes. Possible overlapping between IR and Raman bands is well documented in previous literature.[59,60] For example, in the α-PbO IR spectrum, mode A_{2u} falls over the E_u one forming a broad band around 290[60] and 278 cm^{-1}.[59] Reflectance IR spectroscopy[59] successfully resolved the single bands in two distinct peaks (here, only transversal modes are discussed): that is, 470 cm^{-1} (A_{2u}) and 243 cm^{-1} (E_u, see Table 4). A rather large discrepancy is seen for the PBE A_{2u} mode (−83 cm^{-1}), which gets even worse with PBE-DC2 (−104 cm^{-1}). For the E_u mode, a much better agreement is seen with some influence of dispersion. In general, the inclusion of dispersive interactions via PBE-DC2 does not introduce substantial changes to the IR and Raman modes. As noticed by Ugliengo et al.,[61] there is no direct dispersion correction to the vibrational frequencies as they only change because of a different optimum geometry.

Theoretical LDA IR frequencies (see Table 4)[50] agree with our PBE and PBE-DC2 data. Degeneracy occurring for E_u modes makes them more intense than the A_{2u} peak as demonstrated by PBE and PBE-DC2 IR intensities. PBE and PBE-DC2 Raman frequencies are in much better agreement with experimental data than the IR ones. This excludes the E_g mode, which suffers a large ipso-chromic shift inverting the experimental order $B_{1g} > E_g$. However, the experimental intensity of this mode is very weak.[59]

4.3.2. β-PbO. For β-PbO, IR active modes are all ungerade (antiphase deformation) such as $3B_{2u}$, $3B_{3u}$, and B_{1u}, whereas the Raman activities are all gerade (in phase deformation) $4B_{1g}$, $2B_{2g}$, $2B_{3g}$, and $4A_g$. $2A_u$ modes are neither IR nor Raman active, hence, they will be not discussed. In Figure 5 are only shown the graphical atomic displacements of certain modes,

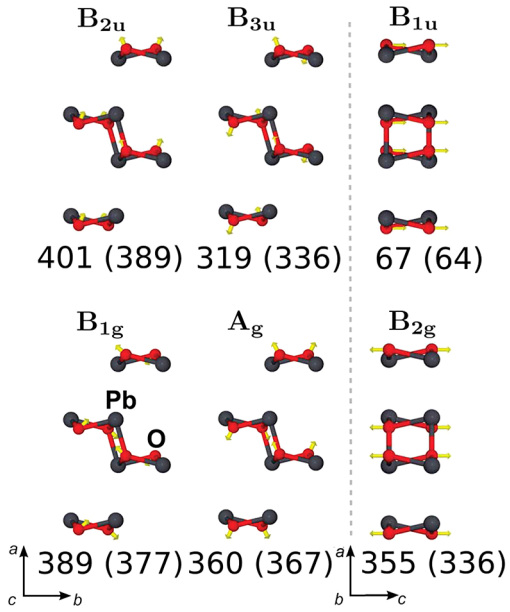

Figure 5. Selection of active IR (on the top part) and Raman (on the bottom part) modes for β-PbO in cm^{-1}. The dashed line separates modes with different cell orientations. PBE-DC2 values are in brackets.

dx.doi.org/10.1021/jp3036988 | J. Phys. Chem. C 2012, 116, 21514−21522

Table 5. IR, Raman (R) Frequencies, in cm^{-1}, of α-PbO[a]

		ν					$\Delta\nu$		IR int.	
irep.	A	PBE	PBE-DC2	LDA[b]	E IR[c]	E R[c]	PBE	PBE-DC2	PBE	PBE-DC2
B_{2u}	IR	401	389	418	356		45	33	1391	1913
B_{1g}	R	389	377			385	4	−8		
A_g	R	360	367			349	11	18		
B_{2g}	R	355	336							
B_{2u}	IR	350	337	281/360	290		60	47	65	168
B_{3u}	IR	319	336	281/360	424/500		−181	−164	816	795
B_{1g}	R	310	313		250		60	63		
A_u	*i*	293	272							
A_g	R	279	270		289		−10	−19		
B_{3u}	IR	266	270	281/360	424		−158	−154	1219	1538
B_{3g}	R	222	235		171		51	64		
B_{2u}	IR	122	136		146		−24	−10	0	0
A_g	R	90	100		87		3	13		
B_{2g}	R	86	111		72		14	39		
B_{1g}	R	68	74		52		16	22		
B_{1u}	IR	67	64	78			−11	−14	2947	3321
A_u	*i*	65	83							
B_{3u}	IR	59	64						14	21
B_{3g}	R	56	76							

[a]Simulated intensities are only available for IR modes and are expressed in km mol^{-1}. Irep. is for irreducible representation, A is for activity, *i* is for inactive, int. is for intensity, and E is for experimental. Experimental IR and Raman frequencies values were measured by Adams et al.,[59] while theoretical values are only available for IR.[50] Whenever the experimental data is available, $\Delta\nu$ is calculated from this value. [b]Reference 50, PP-PW. [c]Reference 59, single crystal specimen at 295 K.

which fall at high-frequencies (500−200 cm^{-1}, exception is B_{1u}), that is, B_{2u} and B_{3u} for IR and B_{1g}, A_g, B_{2g}, and A_u for Raman modes.

An electric vector along *b* stimulates the B_{2u} modes, whereas a vector along *c* stimulates the B_{1u}; both vectors lay normal to the planes and are formed by the sandwiched arrangement of β-PbO (see Figure 5 and Figure 1b). Table 5 compares the present results with previous experimental works of the IR (along with simulated intensities) and Raman frequencies.

Adams and Stevens[59] assigned the main bands to their respective vibrational modes. Simulated frequencies below 68 cm^{-1} are reported in Table 5; however, they were not revealed experimentally. PBE and PBE-DC2 IR frequencies are similar to both experimental[59] and previous theoretical ones.[50] This is particularly true for the B_{2u} mode that suffers a small ipsochromic shift from the experimental value. Waghmare and Rabe found the same trend using a PP-PW approach.[50] Puzzling is the comparison of the B_{3u} modes, which seems underestimated by PBE by 181 cm^{-1}. This mode involves the motion of both Pb and O right across the layered structure (see Figure 5). The PBE-DC2 slightly improves this mode. The correct assignment of the B_{3u} modes is also not very clear from the experimental point of view because other modes such A_g and B_{3g} would overlap and mix with these modes. Adams and Stevens claimed that these bands could be assigned to overtones.[59] Waghmare and Rabe addressed this issue reporting a possible spectral window of 281−360 cm^{-1} [50] underestimating the experimental values. Raman frequencies agree very well with those assigned experimentally. The B_{1g} mode suffers a small upshift. The other modes fall below this threshold concluding that our simulation describe the Raman spectrum with good accuracy.

5. CONCLUSION

We demonstrated the use of LCAO approach within the DFT framework to address different properties of lead monoxide polymorphs. We tested several GGA and hybrid functionals to predict as well as possible the PbO geometrical properties. Among the adopted functionals, PBE is the best option as Becke's exchange based functionals (BLYP and B3LYP) largely overestimated the cell parameters. The correct geometry is, however, only reproduced when the dispersion interaction is included. In that respect, a new strategy to reparametrize Grimme's coefficients for Pb and O in PbO is presented, which can be extended also to other semi-ionic solids. This is based on the use of ab initio polarizabilities and ionization potentials, which account for the crystalline environments experienced by the ions. The introduction of dispersive interactions was found essential to reproduce the experimental cell parameters for both PbO polymorphs and was shown to be the major component of the interlayer interaction. In accordance with previous computational works, our data justify different anisotropy of the Pb lone pair within the two lead monoxide polymorphs, and this is further confirmed by the quadrupolar coupling constants. Elastic constants clearly show how the α-phase is affected by a larger anisotropy than the β one, which eventually reflects the lone-pair orientation within the two PbO phases. The PBE PbO phonons, at the Γ-point, for both phases are only in moderate agreement with the experiment, and inclusion of dispersion at PBE-DC2 slightly worsens the agreement for the alpha phase while it remains almost the same for the beta one. As anharmonicity should not play a key role for these systems, we suspect that the Grimme's approach to account for dispersion does not improve frequencies as it has only an indirect effect through the change in the equilibrium geometry. Further study is needed to clarify this matter.

■ ASSOCIATED CONTENT

Supporting Information

Derivation of C_6^i parameters for Pb and O in PbO and frequencies for α-PbO with and without BSSE. This material is available free of charge via the Internet at http://pubs.acs.org.

■ AUTHOR INFORMATION

Corresponding Author

*E-mail: canepap@wfu.edu.

Notes

The authors declare no competing financial interest.

■ ACKNOWLEDGMENTS

This research was supported by a UKC Scholarship from University of Kent. The authors would like to acknowledge the use of the UK National Grid Service in carrying out this work. P.C. and P.U. are very thankful to Dr. Marta Corno and Dr. Bartolomeo Civalleri of the Department of Chemistry, University of Torino. We are finally very thankful to both referees for their comments.

■ REFERENCES

(1) Pan, Z. W.; Dai, Z. R.; Wang, Z. L. *Appl. Phys. Lett.* **2002**, *80*, 309.
(2) Sun, P.; Matsuura, N.; Ruda, H. F. *J. Appl. Phys.* **2004**, *96*, 3417–3423.
(3) Murphy, J. E.; Beard, M. C.; Norman, A. G.; Ahrenkiel, S. P.; Johnson, J. C.; Yu, P. R.; Micic, O. I.; Ellingson, R. J.; Nozik, A. J. *J. Am. Chem. Soc.* **2006**, *128*, 3241–3247.
(4) Takaishi, T.; Jin, J.; Uchino, T.; Yoko, T. *J. Am. Chem. Soc.* **2000**, *83*, 2543.
(5) Fujino, S.; Hwang, C. S.; Morinaga, K. *J. Am. Chem. Soc.* **2004**, *87*, 10–16.
(6) McCann, L. I.; Trentelman, K.; Possley, T.; Golding, B. *J. Raman Spectrosc.* **1999**, *30*, 121–132.
(7) Pilania, G.; Tan, D. Q.; Cao, Y.; Venkataramani, V. S.; Chen, Q.; Ramprasad, R. *J. Mater. Sci.* **2009**, *44*, 5249–5255.
(8) Heideman, G.; Noordermeer, J. W. M.; Datta, R. N. *Kautsch. Gummi Kunstst.* **2005**, *58*, 30–42.
(9) Nanda, M.; Tripathy, D. K. *Polym. Polym. Compos.* **2010**, *18*, 417–427.
(10) Cruz, M.; Hernán, L.; Morales, J.; Sánchez, L. *J. Power Sources* **2002**, *108*, 35–40.
(11) Ahuja, R.; Blomqvist, A.; Larsson, P.; Pyykkö, P.; Zaleski-Ejgierd, P. *Phys. Rev. Lett.* **2011**, *106*, 018301.
(12) Watson, G. W.; Parker, S. C. *J. Phys. Chem. B* **1999**, *103*, 1258–1262.
(13) Watson, G. W.; Parker, S. C.; Kresse, G. *Phys. Rev. B* **1999**, *59*, 8481–8486.
(14) Boher, P.; Garnier, P.; Gavarri, J. R.; Hewat, A. W. *J. Solid State Chem.* **1985**, *57*, 343–350.
(15) Evarestov, R. A.; Veryazov, V. A. *Phys. Status Solidi B* **1991**, *165*, 401–410.
(16) Terpstra, H. J.; de Groot, R. A.; Haas, C. *Phys. Rev. B* **1995**, *52*, 11690–11697.
(17) Haussermann, U.; Berastegui, P.; Carlson., S.; Haines, J.; Ledger, J.-M. *Angew. Chem., Int. Ed.* **2001**, *40*, 4624–4628.
(18) Raulot, J.-M.; Baldinozzi, G.; Seshadri, R.; Cortona, P. *Solid State Sci.* **2002**, *4*, 467–474.
(19) French, R. H. *Rev. Mod. Phys.* **2010**, *82*, 1887–1944.
(20) Dion, M.; Rydberg, H.; Schröder, E.; Langreth, D. C.; Lundqvist, B. I. *Phys. Rev. Lett.* **2004**, *92*, 246401.
(21) Thonhauser, T.; Cooper, V. R.; Li, S.; Puzder, A.; Hyldgaard, P.; Langreth, D. C. *Phys. Rev. B* **2007**, *76*, 125112.
(22) Lee, K.; Murray, E. D.; Kong, L.; Lundqvist, B. I.; Langreth, D. C. *Phys. Rev. B* **2010**, *82*, 081101.
(23) Vydrov, O. A.; Van Voorhis, T. *Phys. Rev. Lett.* **2009**, *103*, 063004.
(24) Zhao, Y.; Schultz, N. E.; Truhlar, D. G. *J. Chem. Phys.* **2005**, *123*, 161103.
(25) Zhao, Y.; Truhlar, D. G. *Acc. Chem. Res.* **2008**, *41*, 157–167.
(26) Grimme, S. *J. Comput. Chem.* **2004**, *25*, 1463.
(27) Grimme, S. *J. Comput. Chem.* **2006**, *27*, 1787.
(28) Grimme, S.; Antony, J.; Ehrlich, S.; Krieg, H. *J. Chem. Phys.* **2010**, *132*, 154104.
(29) Tkatchenko, A.; Scheffler, M. *Phys. Rev. Lett.* **2009**, *102*, 073005.
(30) Tkatchenko, A.; DiStasio, R. A., Jr.; Head-Gordon, M.; Scheffler, M. *J. Chem. Phys.* **2009**, *131*, 094106.
(31) Dovesi, R.; Civalleri, B.; Orlando, R.; Roetti, C.; Saunders, V. R. *Reviews in Computational Chemistry*; John Wiley & Sons: New York, 2005; Chapter 1, Vol. *21*, pp 1–126.
(32) Dovesi, R.; Saunders, V. R.; Roetti, C.; Orlando, R.; Zicovich-Wilson, C. M.; Pascale, F.; Civalleri, B.; Doll, K.; Harrison, N. M.; Bush, I. J.; D'Arco, P.; Llunell, M. *CRYSTAL09, User Manual*; University of Turin: Turin, Italy, 2009.
(33) Perdew, J. P.; Burke, B.; Ernzerhof, M. *Phys. Rev. Lett.* **1996**, *77*, 3865–3868.
(34) Perdew, J. P.; Ruzsinszky, A.; Csonka, G. I.; Vydrov, O. A.; Scuseria, G. E.; Constantin, L. A.; Zhou, X.; Burke, K. *Phys. Rev. Lett.* **2008**, *100*, 136406.
(35) Becke, A. *Phys. Rev. A* **1988**, *38*, 3098–3100.
(36) Lee, C.; Yang, W.; Parr, R. G. *Phys. Rev. B* **1988**, *37*, 785–789.
(37) Becke, A. D. *J. Chem. Phys.* **1993**, *98*, 5648–5652.
(38) Adamo, C.; Barone, V. *J. Chem. Phys.* **1999**, *110*, 6158–6170.
(39) Schafer, A.; Horn, H.; Ahlrichs, R. *J. Chem. Phys.* **1992**, *97*, 2571.
(40) Metz, B.; Stoll, H.; Dolg, M. *J. Chem. Phys.* **2000**, *113*, 2563–2567.
(41) Peterson, K. A.; Figgen, D.; Goll, E.; Stoll, H.; Dolg, M. *J. Chem. Phys.* **2003**, *119*, 11099–11112.
(42) Monkhorst, H. J.; Pack, J. D. *Phys. Rev. B* **1976**, *13*, 5188–5192.
(43) Perger, W. F.; Criswell, J.; Civalleri, B.; Dovesi, R. *Comput. Phys. Commun.* **2009**, *180*, 1753–1759.
(44) Pascale, F.; Zicovich-Wilson, C. M.; López Gejo, F.; Civalleri, B.; Orlando, R.; Dovesi, R. *J. Comput. Chem.* **2004**, *25*, 888–897.
(45) Giannozzi, P.; Baroni, S.; Bonini, N.; Calandra, M.; Car, R.; Cavazzoni, C.; Ceresoli, D.; Chiarotti, G. L.; Cococcioni, M.; Dabo, I.; Dal Corso, A.; Fabris, S.; Fratesi, G.; de Gironcoli, S.; Gebauer, R.; Gerstmann, U.; Gougoussis, C.; Kokalj, A.; Lazzeri, M.; Martin-Samos, L.; Marzari, N.; Mauri, F.; Mazzarello, R.; Paolini, S.; Pasquarello, A.; Paulatto, L.; Sbraccia, C.; Scandolo, S.; Sclauzero, G.; Seitsonen, P.; Smogunov, A.; Umari, P.; Wentzcovitch, R. M. *J. Phys.: Condens. Matter* **2009**, *21*, 395502 (2009).
(46) Canepa, P.; Hanson, R.; Ugliengo, P.; Alfredsson, M. *J. Appl. Crystallogr.* **2011**, *44*, 225–229.
(47) Conesa, J. C. *J. Phys. Chem. C* **2010**, *114*, 22718–22726.
(48) Allen, J. P.; Scantlon, D. O.; Parker, S. C.; Watson, G. W. *J. Phys. Chem. C* **2011**, *115*, 19916–19924.
(49) Tosoni, S.; Sauer, J. *Phys. Chem. Chem. Phys.* **2010**, *42*, 14330–40.
(50) Waghmare, U.; Rabe, K. In *Materials Fundamentals of Gate Dielectrics*; Demkov, A. A., Navrotsky, A., Eds.; Springer: Netherlands, 2005; pp 215–247.
(51) Wyckoff, R. W. G. *Crystal structures* ;2nd ed.; John Wiley & Sons, Inc., New York, 1964; pp 85–237.
(52) Hill, R. J. *Acta Crystallogr. C* **1985**, *41*, 1281–1284.
(53) Giefers, H.; Porsch, F. *Physica B* **2007**, *400*, 53–58.
(54) Wu, X.; Vargas, M. C.; Nayak, S.; Lotrich, V.; Scoles, G. *J. Chem. Phys.* **2001**, *115*, 8748.
(55) Kaufmann, E. N.; Vianden, R. J. *Rev. Mod. Phys.* **1979**, *51*, 161–214.
(56) Friedemann, S.; Heinrich, F.; Haas, H.; Tröger, W. *The Nuclear Quadrupole Interaction of ^{204m}Pb in Lead Oxides*; Springer: Netherlands, 2004; Vol. *159*, pp 313–322.
(57) Pyykkö, P. *Z. Naturforsch.* **1992**, *47a*, 189–196.

(58) Le Bellac, D.; Kiat, J.-M.; Hedoux, A.; Garnier, P.; Grebille, D.; Guinet, Y.; Noiret, I. *Ferroelectrics* **1992**, *125*, 215−220.
(59) Adams, D.; Stevens, D. *Dalton Trans.* **1976**, *371*, 1096−1103.
(60) Donaldson, J.; Donoghue, M.; Ross, S. D. *Spectrochim. Acta, Part A* **1974**, *30*, 1967−1975.
(61) Ugliengo, P.; Zicovich-Wilson, C. M.; Tosoni, S.; Civalleri, B. *J. Mater. Chem.* **2009**, *19*, 2564−2572.